

Enhanced photocatalytic activity of magnetic core–shell $\text{Fe}_3\text{O}_4@ \text{Bi}_2\text{O}_3$ –RGO heterojunctions for quinolone antibiotics degradation under visible light

Yuanjie Zhu¹ · Jinjuan Xue¹ · Tingting Xu¹ · Guangyu He¹ · Haiqun Chen¹

Received: 7 December 2016 / Accepted: 13 February 2017 / Published online: 24 February 2017
© Springer Science+Business Media New York 2017

Abstract A magnetically separable $\text{Fe}_3\text{O}_4@ \text{Bi}_2\text{O}_3$ –RGO core–shell heterostructured photocatalyst was successfully prepared through a self-assembly method for the first time. The Fe_3O_4 nanoparticles with an average diameter of 200 nm was wrapped by approximately 50 nm thick layer of Bi_2O_3 to form unique $\text{Fe}_3\text{O}_4@ \text{Bi}_2\text{O}_3$ nanospheres, then loaded on the surface of reduced graphene oxide (RGO). Compared with pure Bi_2O_3 and $\text{Fe}_3\text{O}_4@ \text{Bi}_2\text{O}_3$, the as-synthesized $\text{Fe}_3\text{O}_4@ \text{Bi}_2\text{O}_3$ –RGO nanocomposites showed broadened visible light adsorption range, increased charge separation efficiency, excellent photocatalytic activity and cyclic stability for degradation of quinolone antibiotics (QAs) under visible light irradiation. The degradation rate of ciprofloxacin (CIP) with $\text{Fe}_3\text{O}_4@ \text{Bi}_2\text{O}_3$ –RGO photocatalyst could reach 98.3% in 240 min and it was still above 80% after ten photocatalytic reaction cycles. More importantly, benefiting from the introduction of Fe_3O_4 and RGO, the $\text{Fe}_3\text{O}_4@ \text{Bi}_2\text{O}_3$ –RGO nanocomposites could effectively prevent the rapid recombination of photogenerated electron–hole pairs and photocorrosion phenomenon of Bi_2O_3 , which made it become a highly stable and durable photocatalyst. These attractive features make the $\text{Fe}_3\text{O}_4@ \text{Bi}_2\text{O}_3$ –RGO nanocomposites to be a promising photocatalyst for visible light photocatalytic degradation of QAs in water pollutants treatment.

1 Introduction

Antibiotics are significant achievements of the twentieth century in medical science that are widely used in human and animal to prevent and treat microbial infections [1]. It is reported that over 75% of antibiotics are inappropriately abused in healthcare facilities of developing countries, even the western developed countries this proportion nearly reaches 50% [2]. Antibiotic residues have the potential to generate persistent negative environmental impacts even in low concentrations, including pathogen resistance and mutation, perturbations in ecosystem and possible risks to human health through drinking water or food-chain [3, 4], especially synthetic quinolone antibiotics. Therefore, antibiotic residues have increasingly become an serious social and environmental problem around the world.

Semiconductor mediated photocatalysts with superior photocatalytic activity have been hot spot of recent research on antibiotic residues treatment, such as TiO_2 , ZnO, CdS and so on [5–9]. In this aspect, Bi_2O_3 is a very attractive semiconductor because of its conductivity, catalytic activity and narrow band gap (2.8 eV) [10]. However, when pure Bi_2O_3 functioned as a photocatalyst, rapid recombination of photogenerated electron–hole pairs and photocorrosion phenomenon would happen to reduce the photocatalytic activity during the photocatalytic process [11]. Thus, in order to improve the photocatalytic activity of Bi_2O_3 , researchers have developed many different methods, such as ion doping, metal deposition and structure or morphology control to prepare various different Bi_2O_3 -based photocatalysts $\text{Bi}_2\text{O}_3/\text{TiO}_2$, $\text{Bi}_2\text{O}_3/\text{Co}_3\text{O}_4$, $\text{Fe}^{3+}/\text{Bi}_2\text{O}_3$, $\text{Er}^{3+}/\text{Bi}_2\text{O}_3$, $\text{Ti}-\text{Bi}_2\text{O}_3$, $\text{Pt}-\text{Bi}_2\text{O}_3$, $\text{Ag}-\text{Bi}_2\text{O}_3$, α , β , γ - Bi_2O_3 nanosheet, nanosphere or nanoneedle and so on [12–22]. Recently, semiconductor mediated material combined with magnetic carrier

✉ Haiqun Chen
chenhq666@hotmail.com

¹ Key Laboratory of Advanced Catalytic Materials and Technology, Advanced Catalysis and Green Manufacturing Collaborative Innovation Center, Changzhou University, Changzhou 213164, Jiangsu, China

as composite photocatalysts have also been extensively investigated, such as $\text{Fe}_3\text{O}_4/\text{TiO}_2$, $\text{Fe}_3\text{O}_4@\text{Bi}_2\text{O}_3$, $\text{Fe}_3\text{O}_4@\text{ZnO}$ and $\text{Fe}_3\text{O}_4/\text{CdS}$ magnetic core-shell semiconductor composites [23–26]. The Fe^{3+} as electrons acceptor not only made charge separate and transfer effectively, but also endowed composite photocatalysts with magnetic separation ability. However, most of the magnetic binary catalysts have poor visible light absorption property and cyclic stability, limiting their further practical application. Our previous studies showed when ferrite were loaded on the surface of RGO to form $\text{NiFe}_2\text{O}_4\text{-RGO}$, $\text{CoFe}_2\text{O}_4\text{-RGO}$, $\text{ZnFe}_2\text{O}_4\text{-RGO}$ [27–29], high photocatalytic activity of the composites were obtained and could effectively degrade organic pollutants under visible light irradiation. It is attributed to RGO possesses large specific surface area, outstanding electrical conductivity, excellent light adsorption and high chemical and thermal stability. The presence of RGO can sufficiently adsorb visible light and decrease the recombination of photogenerated electrons and holes, making it attractive for pollutants treatment [30–33].

Based on above studies, we designed and fabricated $\text{Fe}_3\text{O}_4@\text{Bi}_2\text{O}_3\text{-RGO}$ heterojunctions photocatalyst via a simple self-assembly strategy. The sunlight illumination conditions were simulated and the performance of $\text{Fe}_3\text{O}_4@\text{Bi}_2\text{O}_3\text{-RGO}$ photocatalyst for visible light photocatalytic degradation of different quinolone antibiotics were carefully examined. The cyclic stability and photocatalytic kinetics of $\text{Fe}_3\text{O}_4@\text{Bi}_2\text{O}_3\text{-RGO}$ photocatalyst for degradation CIP was investigated. Furthermore, a possible mechanism of the photocatalytic reaction was proposed. The results fully certificated magnetic core-shell $\text{Fe}_3\text{O}_4@\text{Bi}_2\text{O}_3\text{-RGO}$ heterojunctions had outstanding photocatalytic activity, excellent cyclic stability, and convenient magnetic separation.

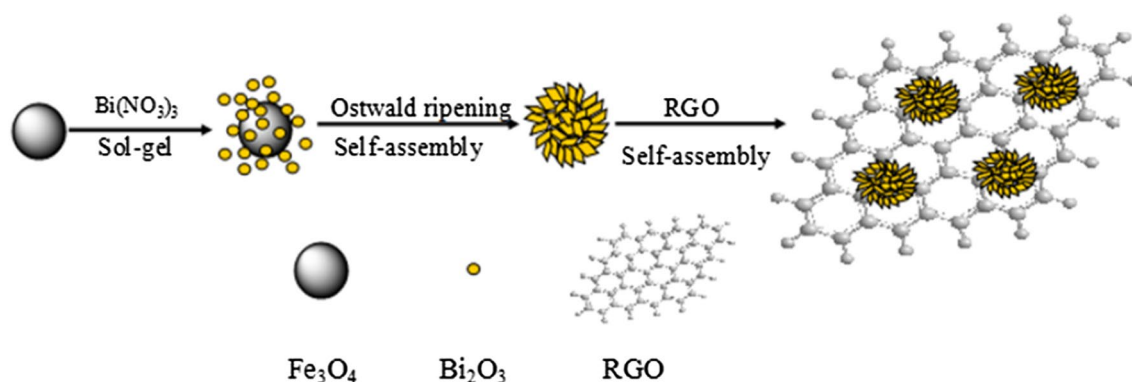
2 Experimental section

2.1 Chemicals

Natural graphite powder (99.9%, 500 mesh), $\text{FeCl}_3\cdot 6\text{H}_2\text{O}$, $\text{Bi}(\text{NO}_3)_3\cdot 5\text{H}_2\text{O}$, quinolone antibiotics (ciprofloxacin, norfloxacin, ofloxacin, moxifloxacin), ethanol, acetonitrile and other materials were purchased from Sinopharm Chemical Reagent Co., Ltd. (China). All chemicals were of analytical grade and used without further purification.

2.2 Synthesis of $\text{Fe}_3\text{O}_4@\text{Bi}_2\text{O}_3\text{-RGO}$ nanocomposites

The modified Hummers' method was adopted to prepare GO [34]. The magnetic Fe_3O_4 nanoparticles were synthesized by a solvothermal method according to the method reported by Li et al. [35]. The typical preparation process of $\text{Fe}_3\text{O}_4@\text{Bi}_2\text{O}_3\text{-RGO}$ nanocomposites is illustrated in Scheme 1. $\text{Bi}(\text{NO}_3)_3\cdot 5\text{H}_2\text{O}$ (1.46 g, 3 mmol) was dissolved in 100 mL ethanol by vigorous stirring for 10 min. The as-synthesized magnetic Fe_3O_4 nanoparticles (0.05 g) were added in above solution and sonicated for 30 min. Then the mixture was stirred and heated to 40°C , and NaOH solution (6 M) was dropped to the mixed solution to adjust pH to 12. After thermostatic stirring for 4 h, the sample was separated magnetically and washed three times with deionized water and ethanol to remove redundant ions and impurities, then vacuum dried at 60°C for 12 h and obtained pink powder of $\text{Fe}_3\text{O}_4@\text{Bi}_2\text{O}_3$. After that 0.1 g $\text{Fe}_3\text{O}_4@\text{Bi}_2\text{O}_3$ was added to the RGO dispersion (GO dispersion of hydrazine hydrate reduction), then vigorously stirred for 10 h at room temperature. Finally, the black powder $\text{Fe}_3\text{O}_4@\text{Bi}_2\text{O}_3\text{-RGO}$ nanocomposites was obtained by the same separation, washing and dry procedures as the treatment of $\text{Fe}_3\text{O}_4@\text{Bi}_2\text{O}_3$. For comparison, pure Bi_2O_3 was synthesized by the same method in the absence of Fe_3O_4 .



Scheme 1 Schematic illustration of the formation mechanism of $\text{Fe}_3\text{O}_4@\text{Bi}_2\text{O}_3\text{-RGO}$ nanocomposites

2.3 Characterization

Fourier transform infrared (FTIR) spectra were recorded on a Thermo Nicolet 370 spectrometer using pressed KBr pellets. X-ray diffraction (XRD) patterns were obtained by a Rigaku D/Max 2000 powder diffractometer (Japan) with Cu K_α radiation at a scan rate of 0.02°/s (2 θ). Transmission electron microscopy (TEM) images were taken with a JEOL JEM-2100 microscope with the equipment of energy-dispersive X-ray analysis (EDS) (Hitachi, Japan). Scanning electron microscopy (SEM) images were taken with a JSM-7001F microscope. Zeta potentials were measured by dynamic light scattering (Malvern Nano-ZS, U.K.). EIS measurements were carried out with Solartron 1255B Frequency Response Analyzer (Solartron Inc., UK). UV–vis diffuse reflectance spectra (UV–vis DRS) were recorded on a UV-2700 spectrophotometer (Shimadzu, Japan) equipped with an integrating sphere using BaSO₄ as the reflectance sample. Surface electronic states were analyzed on a X-ray photoelectron spectroscopy (XPS, Perkin-Elmer PHI 5000C ESCA system). Photoluminescence (PL) spectra were measured using a Jobin Yvon SPEX Fluorolog 3P spectroscopy.

2.4 Photocatalytic tests

Photocatalytic experiments were carried out in XPA photochemical reactor (Xujiang machine plant, Nanjing) with a 500 W Xe lamp, and 420 nm cutoff filters was used to eliminate UV and establish only visible light illumination. 0.01 g photocatalyst was dispersed in 40 mL CIP solution (20 mg/L) in a quartz tube, and the reaction temperature was maintained at 25 °C by circulating water. Before irradiating, the solution was stirred in the darkness for 90 min to ensure the adsorption/desorption equilibrium of CIP on the surface of photocatalyst. When the light was on, the reaction solution of 3 mL was taken every 30 min interval and centrifuged to remove essentially catalyst. The photocatalytic activity was monitored using the high performance liquid chromatograph (HPLC; Shimadzu LC-20A, Japan), including Eclipse XDB-C18 (150 mm × 4.6 mm, 5 μ m) chromatographic column, mobile phase of acetonitrile: (0.2 V%) formic acid aqueous solution = 20: 80 (V) and the detection wavelength $\lambda = 277$ nm. According to the changes of peak area in the retention time $t_R = 8.83$ min, the changes of CIP concentration were determined in photocatalytic reaction.

3 Results and discussion

3.1 Structural and morphological characteristics

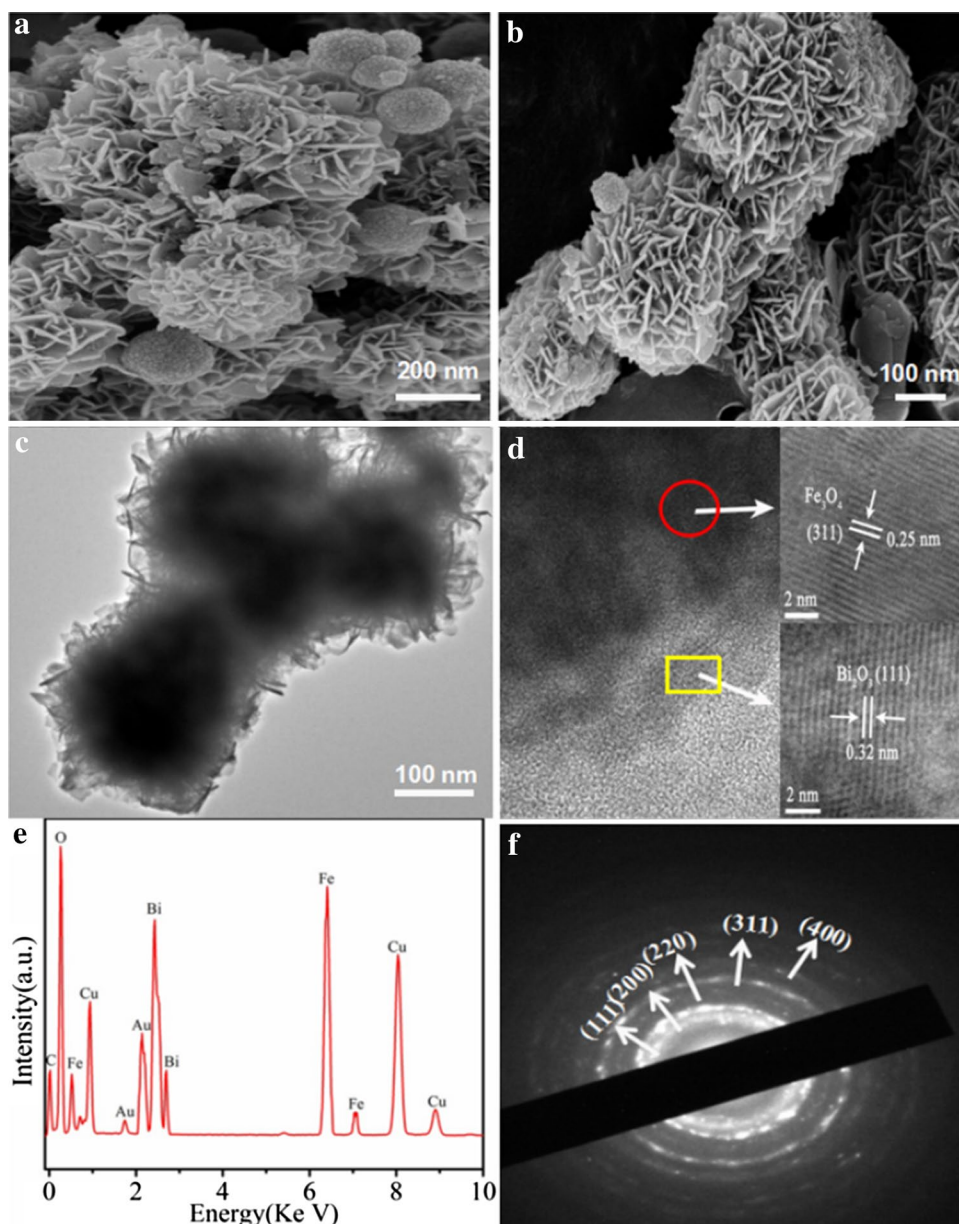
The FESEM images of Fe₃O₄@Bi₂O₃ and Fe₃O₄@Bi₂O₃-RGO are shown in Fig. 1a, b. As can be seen, a

little amount uncovered Fe₃O₄ nanoparticles had an average diameter of 200 nm and a relatively smooth surface and the flowerlike Fe₃O₄@Bi₂O₃ nanospheres with an average diameter of 300 nm were well decorated on the RGO sheets to form the Fe₃O₄@Bi₂O₃-RGO nanocomposites. In order to observe the morphologies and structures more clearly, the as-prepared samples were further characterized through TEM and HRTEM. Figure 1c indicated the Fe₃O₄ nanoparticles was wrapped by approximately 50 nm thick layer of Bi₂O₃ to form the special core-shell structure, which the dark regions represented the Fe₃O₄ core and the bright areas were the Bi₂O₃ shell. The lattice spacings of 0.32 and 0.25 nm are observed in Fig. 1d of HRTEM corresponding to the crystal plane Bi₂O₃ (111) and Fe₃O₄ (311), respectively. The EDS spectrum shown in Fig. 1e proved the Fe₃O₄@Bi₂O₃-RGO nanocomposites contain C, O, Fe, and Bi elements. The appearance of another two metal elements of Au and Cu is due to the spraying of copper mesh. The SAED pattern in Fig. 1f showed diffraction rings (111), (200), (220), (311) and (400), which correspond to Bi₂O₃ different crystal planes, indicating the perfect formation of Bi₂O₃ crystal structure.

The FTIR spectra of GO, Fe₃O₄, and Fe₃O₄@Bi₂O₃-RGO are shown in Fig. 2a. As expected, the FTIR spectra of GO and Fe₃O₄ are consistent with those previous works [36–38]. Compared with GO and Fe₃O₄, new stretching vibration appeared at about 500 cm⁻¹ in the FTIR spectrum of the Fe₃O₄@Bi₂O₃-RGO, which can be ascribed to Bi–O band. Moreover, it is also clearly find that the bands at 1716, 1380, and 1090 cm⁻¹ corresponding to the oxygen-containing functional groups disappeared, suggesting that GO had been reduced to RGO. Figure 2b shows the XRD patterns of Fe₃O₄, Bi₂O₃, and Fe₃O₄@Bi₂O₃-RGO. In the XRD pattern of Fe₃O₄, the diffraction peaks at $2\theta = 30.04^\circ$, 35.38° , 43.10° , 53.44° , 56.90° , and 62.46° correspond to (220), (311), (400), (422), (511), and (440) planes of Fe₃O₄ (JCPDS Card No. 88-0315), respectively. For pure Bi₂O₃, the diffraction peaks at $2\theta = 24.70^\circ$, 28.48° , 32.52° , 46.78° , and 55.01° can be indexed to the (110), (111), (200), (220), and (311) planes of Bi₂O₃ (JCPDS Card No. 71-0464), respectively. All the diffraction peaks of Fe₃O₄ and Bi₂O₃ can be observed in the Fe₃O₄@Bi₂O₃-RGO sample, indicating the perfect formation of Bi₂O₃ crystal structure, this result is consistent with the SAED pattern (Fig. 1f). But in the absence of the typical diffraction peak of RGO (002), it indicates that the formation process of Fe₃O₄@Bi₂O₃ nanospheres did not destroy the characteristic structure of Fe₃O₄, and the Fe₃O₄@Bi₂O₃ nanospheres were successfully loaded on the surface of RGO that would undermine the orderly stack.

For further confirm the Fe₃O₄@Bi₂O₃ nanospheres were well decorated on the surface of RGO sheets, the as-obtained samples were characterized by XPS. In Fig. 2c, it

Fig. 1 FESEM images of **a** $\text{Fe}_3\text{O}_4@ \text{Bi}_2\text{O}_3$, and **b** $\text{Fe}_3\text{O}_4@ \text{Bi}_2\text{O}_3\text{-RGO}$, **c** TEM and **d** HRTEM images of $\text{Fe}_3\text{O}_4@ \text{Bi}_2\text{O}_3$, **e** EDS spectrum and **f** SAED pattern taken from the edge of $\text{Fe}_3\text{O}_4@ \text{Bi}_2\text{O}_3\text{-RGO}$



clearly find that no peaks of other elements are observed except Bi, Fe, C and O, indicating the high purity of the nanocomposites and this result is consistent with the EDS spectrum (Fig. 1e). Figure 2d depicts Bi $4f_{7/2}$ and Bi $4f_{5/2}$ peaks lie at 159.2 and 164.6 eV, certifying the form of Bi_2O_3 crystals [25]. In Fig. 2e, it can be found that the oxygen-containing functional groups on the GO are reduced and the result is consistent with the FTIR and XRD. Figure 2f shows two main peaks with binding energies of 710.3 and 723.9 eV that are respectively assigned to Fe $2p_{3/2}$ and Fe $2p_{1/2}$, indicating the Fe^{2+} (FeO) and Fe^{3+} (Fe_2O_3) peaks are typical characteristics of the Fe_3O_4 structure [38].

The zeta-potential of RGO dispersed in ethanol by ultrasonication was about -20 mV (Fig. 3a). With the content

of $\text{Fe}_3\text{O}_4@ \text{Bi}_2\text{O}_3$ increased to 40–70%, the zeta potential was shifted to values in the 12–17 mV range. These results evidence that the negatively charged surface of the RGO can attract the $\text{Fe}_3\text{O}_4@ \text{Bi}_2\text{O}_3$ nanoparticles and then these nanoparticles are anchored to the surface of RGO [39]. Thus, this self-assembly strategy allows an intimate mixture between RGO layers and $\text{Fe}_3\text{O}_4@ \text{Bi}_2\text{O}_3$ nanoparticles. Additionally, the rate capability of $\text{Fe}_3\text{O}_4@ \text{Bi}_2\text{O}_3\text{-RGO}$ nanocomposites is improved and confirmed by electrochemical impedance spectroscopy (EIS) measurement at fully discharged states (Fig. 3b). The results of EIS verify that charge transfer resistance of $\text{Fe}_3\text{O}_4@ \text{Bi}_2\text{O}_3\text{-RGO}$ is much lower than that of $\text{Fe}_3\text{O}_4@ \text{Bi}_2\text{O}_3$. It is confirmed that introduction of RGO in the nanocomposite promoted

Fig. 2 **a** FTIR spectra of GO, Fe₃O₄, and Fe₃O₄@Bi₂O₃-RGO, **b** XRD patterns of RGO, Fe₃O₄, Bi₂O₃, and Fe₃O₄@Bi₂O₃-RGO, **c** XPS full spectra of Fe₃O₄@Bi₂O₃-RGO and **d** Bi 4f, **e** C 1s, and **f** Fe 2p

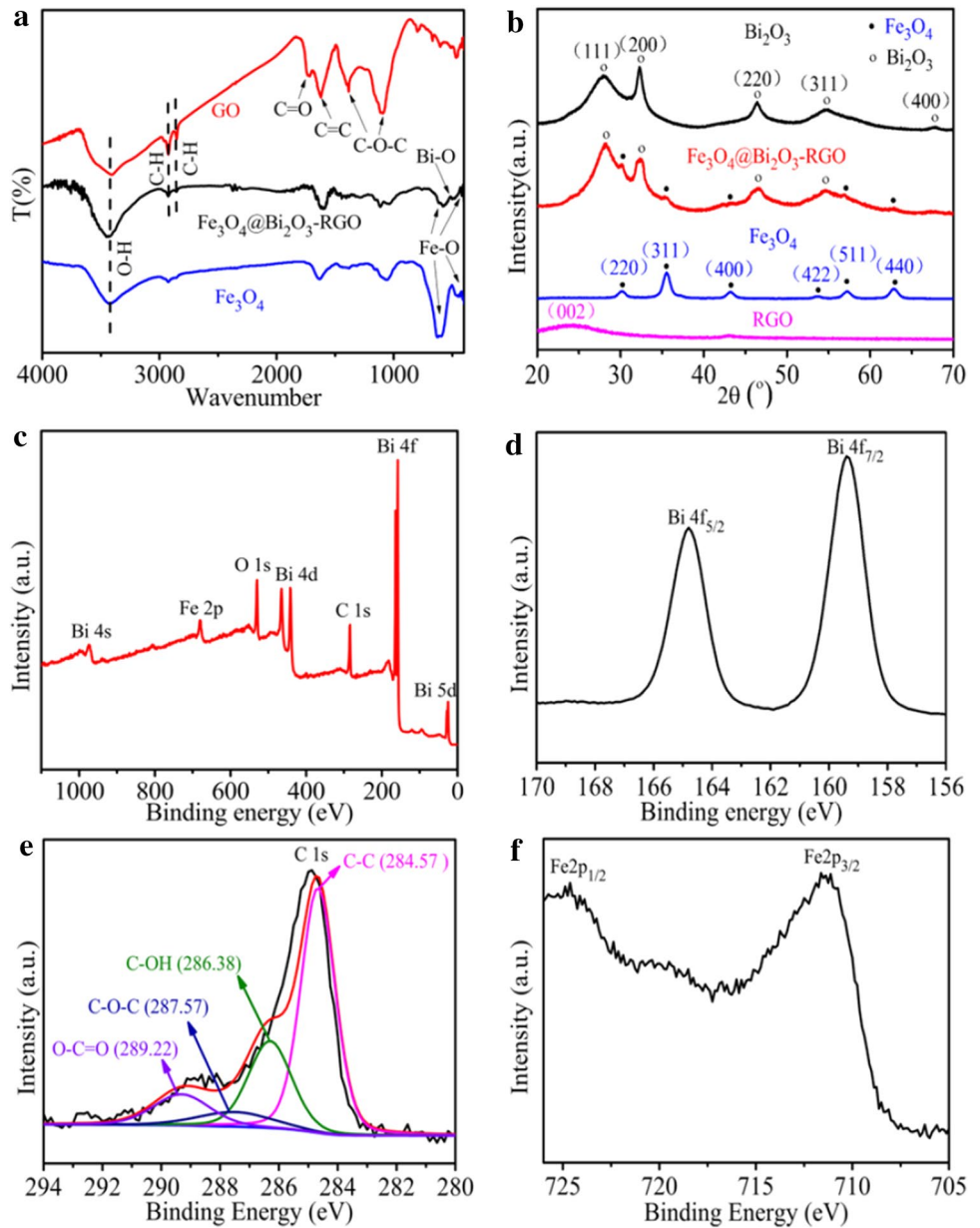
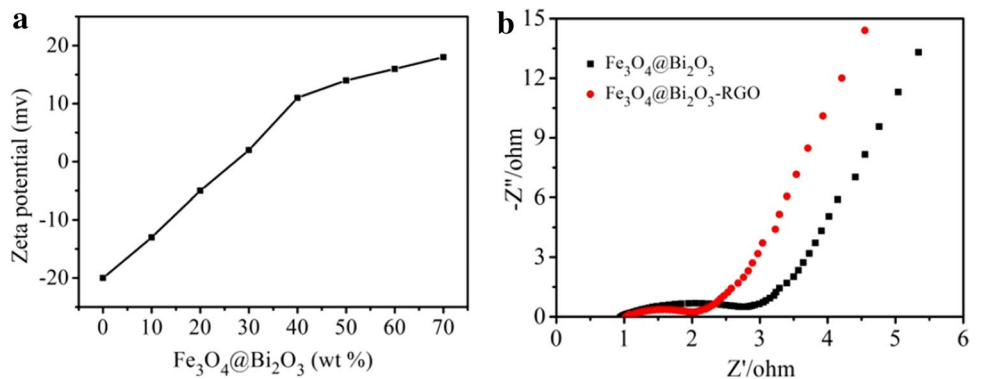


Fig. 3 **a** Zeta potential of Fe₃O₄@Bi₂O₃-RGO as a function of percentage of Fe₃O₄@Bi₂O₃, **b** EIS spectroscopy of Fe₃O₄@Bi₂O₃ and Fe₃O₄@Bi₂O₃-RGO



the electron transport and effectively separated of the photogenerated electron–hole pairs [40].

The optical absorption property of photocatalysts played an important role in the photocatalytic process and were measured by UV–vis DRS. As shown in Fig. 4a, pure Bi_2O_3 had a strong absorption in UV region yet a very weak absorption in the visible light region. When combined with Fe_3O_4 , the $\text{Fe}_3\text{O}_4@ \text{Bi}_2\text{O}_3$ nanospheres showed a better absorption property than pure Bi_2O_3 in the visible light region. Moreover, the $\text{Fe}_3\text{O}_4@ \text{Bi}_2\text{O}_3$ -RGO nanocomposites exhibited a strong absorption ability in the whole UV–vis light range. Due to the Fe_3O_4 can improve the photosensitive of nanocomposites and RGO itself has large surface area and excellent optical absorption property, the decoration of $\text{Fe}_3\text{O}_4@ \text{Bi}_2\text{O}_3$ nanoparticles on RGO sheets not only functionalizes the nanocomposites but also acts as the spacer to partially prevent the aggregation of the RGO sheets [41], the $\text{Fe}_3\text{O}_4@ \text{Bi}_2\text{O}_3$ -RGO nanocomposites can take full advantage of sunlight and would exhibit good photocatalytic activity under visible light irradiation. Additionally, the PL emission intensity is related to the recombination of the photogenerated electron–hole pair [42, 43]. The PL spectrum of Bi_2O_3 , $\text{Fe}_3\text{O}_4@ \text{Bi}_2\text{O}_3$, and $\text{Fe}_3\text{O}_4@ \text{Bi}_2\text{O}_3$ -RGO are shown in Fig. 4b. It can be seen the spectrum exhibited a broad emission band in the 340–480 nm range and appeared absorption peak at 435 nm, which was attributed to luminescence from localized surface states due to the recombination of the photogenerated electron–hole pairs. When combined with Fe_3O_4 , the Fe^{3+} ions could be used as photoexcited electronic acceptor to prevent the fast recombination of photogenerated charge carriers and the PL intensity of $\text{Fe}_3\text{O}_4@ \text{Bi}_2\text{O}_3$ nanospheres would decrease [44]. When the RGO was introduced, due to the superior electronic conductivity of RGO, the PL intensity of the $\text{Fe}_3\text{O}_4@ \text{Bi}_2\text{O}_3$ -RGO nanocomposites was significantly quenched, implying that the recombination of photogenerated electrons and holes was significantly inhibited. The result indicated that the recombination of photogenerated charge carriers was significantly inhibited and the $\text{Fe}_3\text{O}_4@$

Bi_2O_3 -RGO nanocomposites would have excellent photocatalytic activity.

3.2 Photocatalytic activity

The method of HPLC was used to detect the change of peak area for reflecting the changes of CIP concentration in photocatalytic process. As shown in Fig. 5, the test results more intuitive illustration of the $\text{Fe}_3\text{O}_4@ \text{Bi}_2\text{O}_3$ -RGO nanocomposites have excellent photocatalytic activity for CIP degradation under visible light.

It is well known that the adsorption activity of photocatalysts is a precondition for photocatalytic degradation organic pollutants. Due to RGO has large specific surface area, that adsorption activity of $\text{Fe}_3\text{O}_4@ \text{Bi}_2\text{O}_3$ -RGO for organic pollutants will be enhanced with the increase of RGO content. Figure 6a, b show RGO in the $\text{Fe}_3\text{O}_4@ \text{Bi}_2\text{O}_3$ -RGO nanocomposites plays an important role for the adsorption capacity of CIP and adsorption equilibrium could be achieved within 90 min. In the consideration of the cost, 30 wt% RGO is selected as the appropriate content and the adsorption rate is about 25%. Figure 6c, d show photocatalytic activity the $\text{Fe}_3\text{O}_4@ \text{Bi}_2\text{O}_3$ -RGO

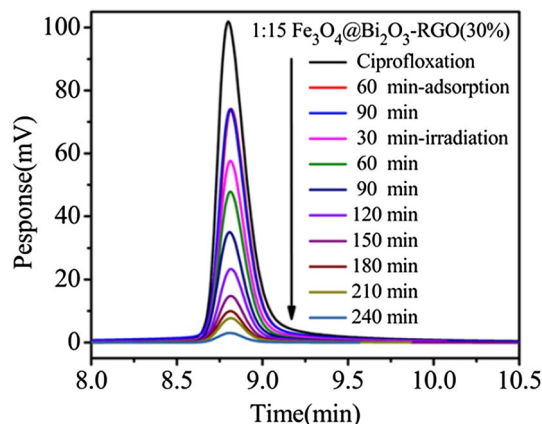


Fig. 5 HPLC spectrum of $\text{Fe}_3\text{O}_4@ \text{Bi}_2\text{O}_3$ -RGO degradation CIP under visible light irradiation

Fig. 4 **a** UV–vis DRS and **b** PL spectra of Bi_2O_3 , $\text{Fe}_3\text{O}_4@ \text{Bi}_2\text{O}_3$ and $\text{Fe}_3\text{O}_4@ \text{Bi}_2\text{O}_3$ -RGO

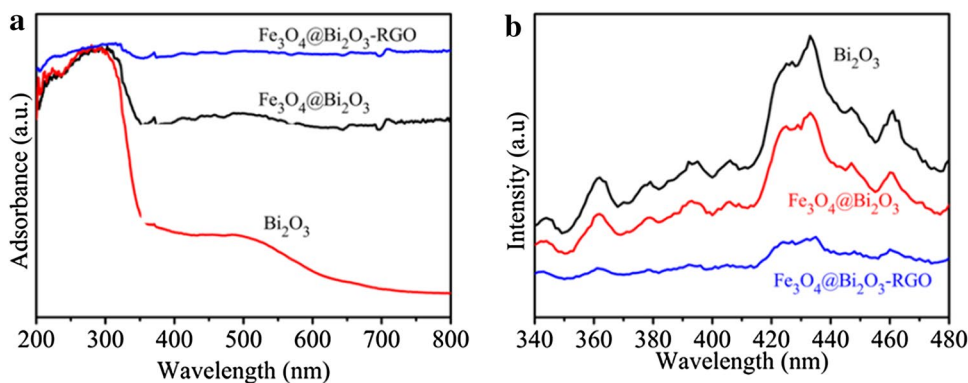
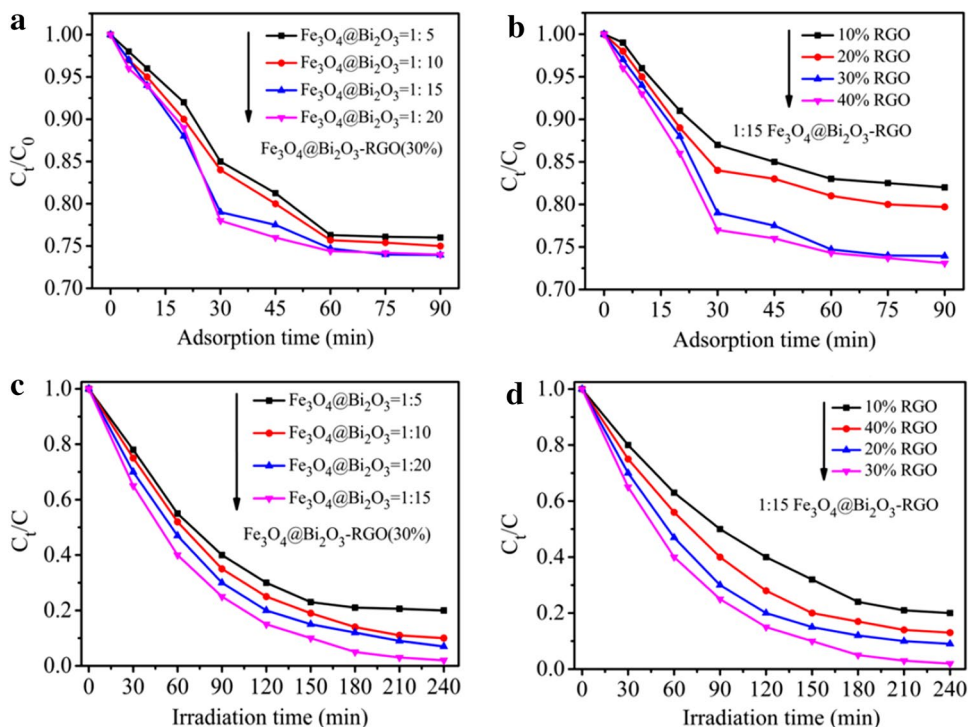


Fig. 6 Adsorption activities of **a** different mass ratios and **b** different RGO contents, photocatalytic properties of **c** different mass ratios and **d** different RGO contents



nanocomposites can be enhanced with the increase of Bi_2O_3 or RGO content. However, excessive content of Bi_2O_3 or RGO in the $\text{Fe}_3\text{O}_4@ \text{Bi}_2\text{O}_3\text{-RGO}$ nanocomposites will be stacked together and decrease active sites to reduce the photocatalytic activity. When RGO content is 30 wt% and the mass ratio of Fe_3O_4 and Bi_2O_3 reaches 1:15, the $\text{Fe}_3\text{O}_4@ \text{Bi}_2\text{O}_3\text{-RGO}$ nanocomposites have the most outstanding photocatalytic activity for degradation CIP and the degradation rate is about 98.3% in 240 min.

It is found $\text{Fe}_3\text{O}_4@ \text{Bi}_2\text{O}_3\text{-RGO}$ nanocomposites have the most outstanding photocatalytic activity through a series of comparative experiments and the degradation rate surprisingly reaches 98.3% after visible light irradiated for 240 min, as shown in Fig. 7a. In the absence of light and catalyst conditions, the pollutants themselves hardly degradation. When using pure Bi_2O_3 as a photocatalyst for degradation CIP, the degradation rate is about 35.5% in 240 min. Whereas both $\text{Fe}_3\text{O}_4@ \text{Bi}_2\text{O}_3$ and $\text{Bi}_2\text{O}_3\text{-RGO}$ show a general visible light photocatalytic property and the degradation rate reaches 49.6 and 80.2% within 240 min, respectively. The photocatalytic activity of Fe_3O_4 itself is poor, so the degradation rate of Fe_3O_4 and $\text{Fe}_3\text{O}_4\text{-RGO}$ are only 17.2 and 36.4%, respectively. Moreover, the reaction rates of different catalysts are shown in Fig. 7b. Obviously, the photocatalytic degradation rate of the $\text{Fe}_3\text{O}_4@ \text{Bi}_2\text{O}_3\text{-RGO}$ nanocomposites is over 1.6 times faster than that of the $\text{Bi}_2\text{O}_3\text{-RGO}$, about two times faster than that of the $\text{Fe}_3\text{O}_4@ \text{Bi}_2\text{O}_3$, and around four times faster than that of pure Bi_2O_3 , also indicating $\text{Fe}_3\text{O}_4@ \text{Bi}_2\text{O}_3\text{-RGO}$

nanocomposites have the most outstanding photocatalytic activity for degradation CIP under visible light. For further explore the photocatalytic activity of the $\text{Fe}_3\text{O}_4@ \text{Bi}_2\text{O}_3\text{-RGO}$ nanocomposites, different quinolone antibiotics are chosen to perform the photocatalytic degradation, as shown in Fig. 7c. It can be found that the degradation rates of different quinolone antibiotics are almost identical. While the reaction rates of different quinolone antibiotics are 0.01778, 0.1444, 0.1222, 0.0083 min^{-1} , respectively, as shown in Fig. 7d. This may be related to the molecular weight of different quinolone antibiotics.

The stability is very important for recycling of the $\text{Fe}_3\text{O}_4@ \text{Bi}_2\text{O}_3\text{-RGO}$ nanocomposites in the aspect of practical application. Figure 8a shows the photocatalytic degradation rate remained above 80% after ten cycles, indicating that the $\text{Fe}_3\text{O}_4@ \text{Bi}_2\text{O}_3\text{-RGO}$ nanocomposites have good cycle stability and do not photocorrode during the photocatalytic degradation of CIP, and the XRD patterns of $\text{Fe}_3\text{O}_4@ \text{Bi}_2\text{O}_3\text{-RGO}$ nanocomposites different photocatalysis times can be seen in Fig. 8b, further confirmed this result.

3.3 Photocatalytic mechanism

The trapping experiments were performed to investigate the roles of active species for further reveal the mechanism of photocatalytic degradation CIP by $\text{Fe}_3\text{O}_4@ \text{Bi}_2\text{O}_3\text{-RGO}$ nanocomposites under visible light irradiation. The different scavengers, such as the ethylenediamine tetraacetic

Fig. 7 **a** Photocatalytic properties and **b** kinetics of different catalysts for degradation CIP; **c** photocatalytic activities and **d** kinetic plots of $\text{Fe}_3\text{O}_4@ \text{Bi}_2\text{O}_3\text{-RGO}$ degradation different quinolone antibiotics under visible light

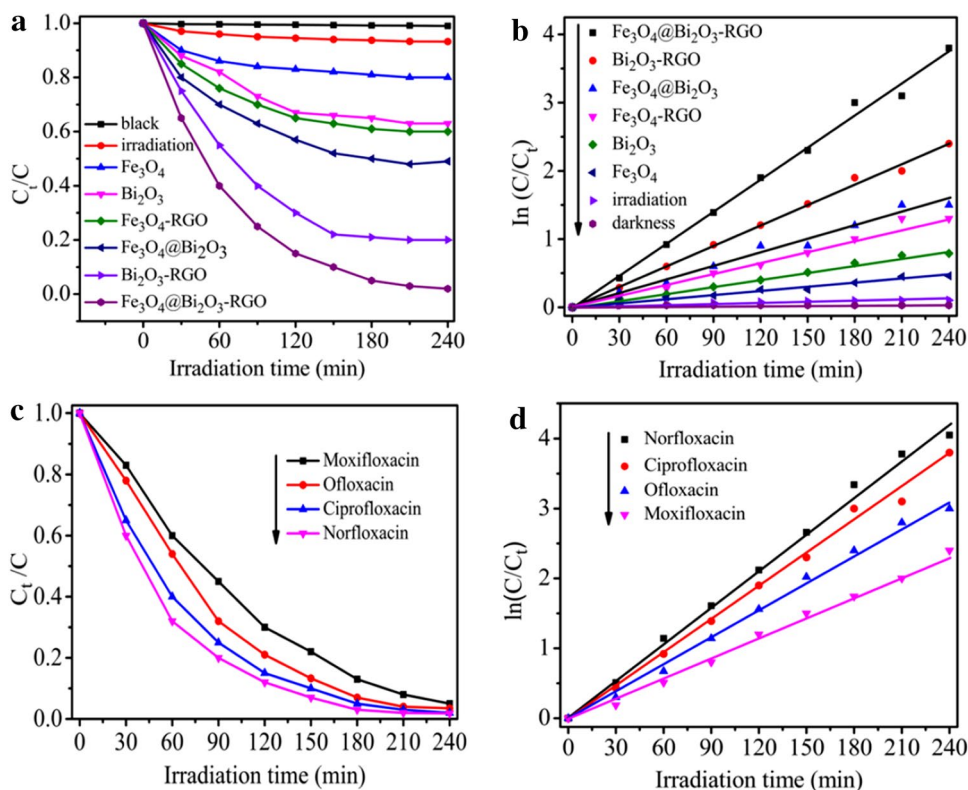
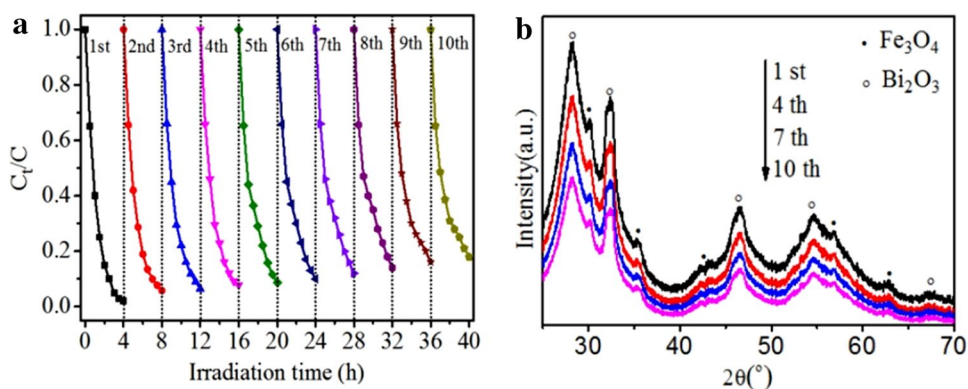


Fig. 8 **a** Cyclic stability and **b** the XRD pattern of different photocatalysis times for $\text{Fe}_3\text{O}_4@ \text{Bi}_2\text{O}_3\text{-RGO}$ nanocomposites



acid disodium salt (EDTA-2Na, h^+ scavenger), benzoquinone (BQ, $\cdot\text{O}_2^-$ scavenger) and *tert*-butanol (*t*-BuOH, $\cdot\text{OH}$ scavenger), were chosen to assess the effects during the photocatalytic degradation processes. As shown in Fig. 9, when separately adding the *t*-BuOH and EDTA-2Na, the photocatalytic degradation rates of CIP with $\text{Fe}_3\text{O}_4@ \text{Bi}_2\text{O}_3\text{-RGO}$ nanocomposites are greatly decreased under visible light, indicating that the main active species were $\cdot\text{OH}$ and h^+ , and $\cdot\text{O}_2^-$ also played a role in the photocatalytic degradation processes.

According to the above results and discussion, a mechanism of photocatalytic degradation process was proposed, as described in Fig. 10. When the $\text{Fe}_3\text{O}_4@ \text{Bi}_2\text{O}_3\text{-RGO}$

nanocomposites are irradiated by visible light, the photoelectrons in the valence band (VB) of Bi_2O_3 can be effectively excited to the conduction band (CB) and generate electron-hole (e^- - h^+) pairs [45]. Being an excellent electron acceptor and conductor, the Fe_3O_4 (Fe^{3+}) [41] and RGO [46] both can promote the effective separation of electron-hole pairs due to the superior electronic conductivity of them. Then the photogenerated electrons react with the dissolved O_2 in the surface of RGO and Fe_3O_4 and transform to $\cdot\text{O}_2^-$ radicals. Meanwhile, corresponding to the photogenerated holes react with the adsorption H_2O molecule to produce $\cdot\text{OH}$ radicals (the major active species). In addition, Fe_3O_4 also is a semiconductor that itself

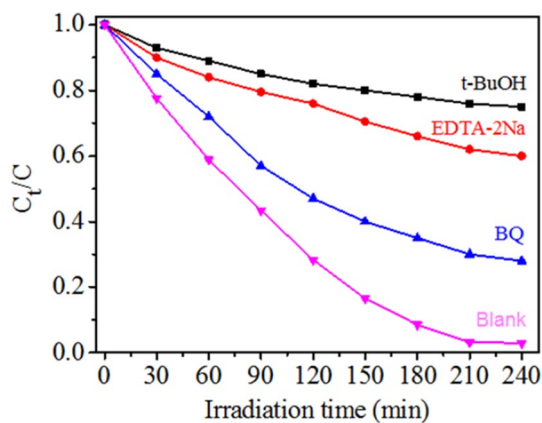


Fig. 9 Different radical scavengers effects of Fe₃O₄@Bi₂O₃-RGO degradation CIP under visible light irradiation

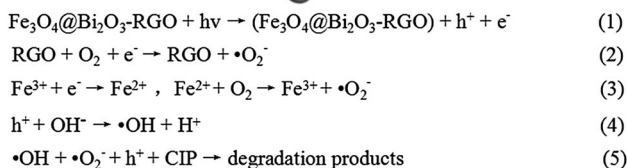
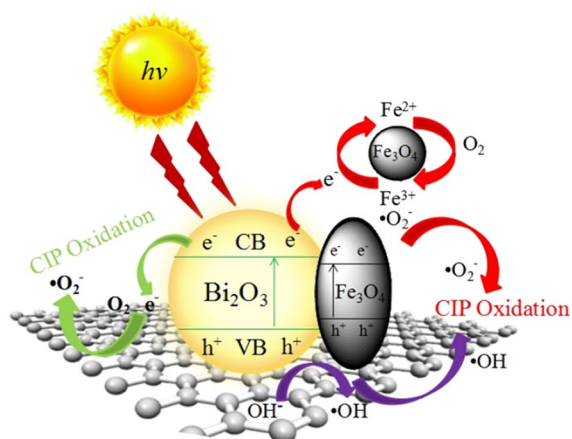


Fig. 10 Schematic diagram of Fe₃O₄@Bi₂O₃-RGO degradation CIP under visible light

can produce photogenerated electrons and holes under visible light irradiation and participate in the photocatalytic reaction [38]. Eventually the active species ($\cdot\text{OH}$, $\cdot\text{O}_2^-$ and h^+) effectively oxidize the organic pollutant of CIP to small inorganic molecules and the photocatalytic degradation processes may be the follow reactions of (1)–(5) [47].

4 Conclusions

In summary, we have successfully prepared magnetic core-shell structure Fe₃O₄@Bi₂O₃-RGO heterojunctions nanocomposites with good visible light absorption

property, outstanding photocatalytic property and excellent cycling stability via self-assembly method. The introduction of RGO in the nanocomposite not only improved optical absorption property, but also promoted the electron transport and effectively separated of the photogenerated electron-hole pairs. At the same time, the presence of Fe₃O₄ also could prevent photo-generated electron-hole pairs recombination and made photocatalyst possess the magnetic separation capability. Moreover, It was found that the photodegradation processes were followed the first order kinetic model and the photocatalytic mechanism of degradation CIP was revealed that there were multiple active species in the photocatalytic reactions.

Acknowledgements The financial supports from the National Natural Science Foundation of China (Nos. 51202020, 51472035, 51572036), the Science and Technology Department of Jiangsu Province (BY2016029-12, BE2014089, BY2015027-18), Changzhou key laboratory of graphene-based materials for environment and safety (CM20153006, CE20160001-2) and the PAPD of Jiangsu Higher Education Institutions are gratefully acknowledged.

References

1. A.K. Sarmah, M.T. Meyer, A. Boxall, *Chemosphere* **65**(5), 759 (2006)
2. G.S. Bbosa, G. Wong, D.B. Kyegombe, J. Ogwalokeng, *Health* **6**(2), 187 (2014)
3. P.T. Hoa, S. Managaki, N. Nakada, H. Takada, A. Shimizu, D.H. Anh, P.H. Viet, S. Suzuki, *Sci. Total. Environ.* **409**(15), 2901(2011)
4. V. Homem, A. Alves, L. Santos, *Sci. Total. Environ.* **408**(24), 6280(2010)
5. E.S. Elmolla, M. Chaudhuri, *Desalination* **252**(1–3), 52(2010)
6. E.S. Elmolla, M. Chaudhuri, *J. Hazard Mater.* **173**(1–3), 449(2010)
7. H.R. Pouretedal, M.A. Hasanali, *Desalin. Water Treat.* **51**(13–15), 2623(2013)
8. J. Fenoll, M.M. Martinez, G. Navarro, N. Vela, S. Navarro, *Chemosphere* **91**(5), 578(2013)
9. S.S. Boxi, S. Paria, *RSC Adv.* **4**(71), 37760(2014)
10. C.H. Wang, C.L. Shao, L.J. Wang, L.N. Zhang, X.H. Li, Y.C. Liu, *J. Colloid Interface Sci.* **333**(1), 248(2009)
11. J.G. Hou, C. Yang, Z. Wang, W.L. Zhou, S.Q. Jiao, H.M. Zhu, *Appl. Catal. B* **142**(11), 511(2013)
12. Z.F. Bian, J. Zhu, S.H. Wang, Y. Cao, X.F. Qian, H.X. Li, J. Phys. Chem. C **112**(16), 6262(2008)
13. S.H. Hsieh, G.J. Lee, C.Y. Chen, J.H. Chen, S.H. Ma, *Top. Catal.* **56**(9), 629(2013)
14. X.H. Wu, W. Qin, L. Li, Y. Guo, Z.Y. Xie, *Catal. Commun.* **10**(5), 604(2009)
15. T.F. Zhou, J.C. Hu, J.L. Li, *Appl. Catal. B* **110**(41), 230(2011)
16. Y. Wang, Y.Y. Wen, H.M. Ding, Y.K. Shan, *J. Mater. Sci.* **45**(5), 1392(2010)
17. Z. Wan, F.M. Feng, J.Z. Li, J.J. He, J.B. Zhong, J. Zeng, *Adv. Mater. Res.* **550–553**, 199(2012)
18. Y.T. Li, Z.F. Zhang, Y.Y. Zhang, X.G. Sun, J.M. Zhang, C.H. Wang, Z. Peng, H.Y. Si, *Ceram. Int.* **40**(8), 13280(2014)
19. X. Zhong, Z. Dai, F. Qin, J. Li, H. Yang, Z. Lu, Y. Liang, R. Chen, *RSC Adv.* **5**(85), 69318(2015)

20. Y.H. Yan, Z.X. Zhou, Y. Cheng, L. Qiu, C. Gao, J.G. Zhou, J. Alloy. Compd. **605**, 108 (2014)
21. W.C. Hao, Y. Gao, X. Jing, W. Zou, Y. Chen, T.M. Wang, J. Mater. Sci. Technol. **30**(2), 143(2014)
22. H.Y. Wang, Y.C. Yang, L. Le, Y. Liu, J.H. Wei, R. Xiong, Solid State Phenom. **181–182**, 335(2011)
23. S.H. Xuan, W.Q. Jiang, X.L. Gong, Y. Hu, Z.Y. Chen, J. Phys. Chem. C **113**(2), 558(2009)
24. W. Yang, S.K. Li, X.R. Xing, F.Z. Huang, Y.H. Shen, A.J. Xie, X.F. Wang, J. Zhang, Chemistry **17**(29), 4808(2011)
25. D.P. Sun, Q. Zou, Y.P. Wang, Y.J. Wang, W. Jiang, F.S. Li, Nanoscale **6**(12), 6562(2014)
26. H. Mcdaniel, M. Shim, ACS Nano **3**(2), 440(2009)
27. Y.S. Fu, H.Q. Chen, X.Q. Sun, X. Wang, AIChE J. **58**(11), 3305(2012)
28. Y.S. Fu, H.Q. Chen, X.Q. Sun, X. Wang, Appl. Catal. B **111**(2), 287(2012)
29. Y.S. Fu, X. Wang, Ind. Eng. Chem. Res. **50**(12), 7218(2011)
30. J.C. Meyer, A.K. Geim, M.I. Katsnelson, K.S. Novoselov, T.J. Booth, S. Roth, Nature **446**(7143), 63(2007)
31. K.S. Novoselov, A.K. Geim, S.V. Morozov, D. Jiang, Y. Zhang, S.V. Dubonos, Science **306**(5696), 669(2004)
32. A.K. Geim, K.S. Novoselov Nat. Mater. **6**(3), 191(2007)
33. J.C. Ireland, P. Klostermann, E.W. Rice, R.M. Clark, Appl. Environ. Microbiol. **59**(5), 1670(1993)
34. W.S. Hummers, R.E. Offeman, J. Am. Chem. Soc. **80**(6), 1339(1958)
35. S.J. Guo, S.J. Dong, E.K. Wang, Chemistry **15**(10), 2424(2009)
36. H. Chen, M.B. Muller, K.J. Gilmore, G.G. Wallace, D. Li, Adv. Mater. **20**(18), 3561(2008)
37. G.Y. He, H.Q. Chen, J.W. Zhu, F.L. Bei, X.Q. Sun, X. Wang, J. Mater. Chem. **21**(38), 14638(2011)
38. G.Y. He, W.F. Liu, X.Q. Sun, Q. Chen, X. Wang, H.Q. Chen, Mater. Res. Bull. **48**(5), 1890(2013)
39. Y. Li, J. Yang, Y.Z. Zhou, N. Zhao, W.W. Zeng, W.W. Wang. Colloids Surf. A **5**(12), 100(2016)
40. Y.Z. Zhou, J. Yang, X.N. Cheng, N. Zhao, L. Sun, H.B. Sun, D. Li. Carbon **50**(12), 4350(2012)
41. Y. Li, J. Yang, S.H. Zheng, W.W. Zeng, N. Zhao, M. Shen, Ceram. Int. **42**, 19096(2016)
42. G. Eda, Y.Y. Lin, C. Mattevi, H. Yamaguchi, H.A. Chen, I.S. Chen, C.W. Chen, M. Chhowalla, Adv. Mater. **22**(4), 509(2010)
43. J.W. Tang, Z.G. Zou, J.H. Ye, Phys. Chem. B **107**(10), 14269(2003)
44. X.H. Feng, H.J. Guo, K. Patel, H. Zhou, X. Lou, Chem. Eng. J. **244**(10), 334(2014)
45. X.F. Chen, J.F. Dai, G.F. Shi, L. Li, G.Y. Wang, H. Yang, J. Alloy. Compd. **649**, 877 (2015)
46. G.Y. He, J.J. Ding, J.G. Zhang, Q.L. Hao, H.Q. Chen, Ind. Eng. Chem. Res. **54**(11) 2867(2015)
47. H.Q. Wang, Z.F. Ye, C. Liu, J.Z. Li, M.J. Zhou, Q.F. Guan, P. Lv, P.W. Huo, Y.S. Yan, Appl. Surf. Sci. **353**, 399 (2015)